

**Global Ocean Surface Velocities from Drifters: Mean, Variance, ENSO Response,
and Seasonal Cycle**

Rick Lumpkin¹ and Gregory C. Johnson²
for *Journal of Geophysical Research–Oceans*

Submitted 24 September 2012

Revised 22 January 2013

¹NOAA/Atlantic Oceanographic and Meteorological Laboratory, 4301 Rickenbacker
Causeway, Miami FL 33149 USA

²NOAA/Pacific Marine Environmental Laboratory, 7600 Sand Point Way NE Bldg. 3,
Seattle WA 98115 USA

e-mail: Rick.Lumpkin@noaa.gov

ABSTRACT

Global near-surface currents are calculated from satellite-tracked drogued drifter velocities on a $0.5^\circ \times 0.5^\circ$ latitude-longitude grid using a new methodology. Data used at each grid point lie within a centered bin of set area with a shape defined by the variance ellipse of current fluctuations within that bin. The time-mean current, its annual harmonic, semiannual harmonic, correlation with the Southern Oscillation Index (SOI), spatial gradients, and residuals are estimated along with formal error bars for each component. The time-mean field resolves the major surface current systems of the world. The magnitude of the variance reveals enhanced eddy kinetic energy in the western boundary current systems, in equatorial regions, and along the Antarctic Circumpolar Current, as well as three large “eddy deserts”, two in the Pacific and one in the Atlantic. The SOI component is largest in the western and central tropical Pacific, but can also be seen in the Indian Ocean basin. Seasonal variations reveal details such as the gyre-scale shifts in the convergence centers of the subtropical gyres and the seasonal evolution of tropical currents and eddies in the western tropical Pacific Ocean. The results of this study are available as a monthly climatology.

1. Introduction

Knowledge of global near-surface currents is important for a variety of uses including ship routing, search and rescue efforts, biological and chemical studies, and both hindcasts and forecasts of the transport and dispersion of floating material including plastic and oil [c.f., *McCord et al.*, 1999; *Davidson et al.*, 2009; *Yoder et al.*, 1994; *Law et al.*, 2010; *Maximenko et al.*, 2012]. Here we apply a new methodology to derive the global distribution of time-mean near-surface ocean currents, their seasonal cycle, their projection onto the Southern Oscillation Index (ENSO), and the variance of eddy fluctuations from a homogeneous data set of global near-surface current observations from the satellite-tracked drifters of the Global Drifter Program (GDP) [*Niiler*, 2001; *Lumpkin and Pazos*, 2007].

Although previous studies have derived a global mean surface velocity field from GDP drifter observations [c.f., *Maximenko et al.*, 2009], they have suffered from contamination by undiagnosed drogue loss for a significant fraction of the data [*Grodsky et al.*, 2011; *Rio et al.*, 2011]. GDP drifters have a drogue (sea anchor) centered at a depth of 15 m to reduce the downwind slip (motion with respect to the current at 15 m depth) to $\sim 0.1\%$ of the wind speed for winds up to 10 m s^{-1} [*Niiler et al.*, 1995] and follow the water within the mixed layer. When this drogue is lost, the downwind slip increases to $\sim 1\text{--}1.5\%$ of the wind speed [*Pazan and Niiler*, 2001; *Poulain et al.*, 2009; *Lumpkin et al.*, 2012]. A recent reanalysis of drogue presence has removed undrogued data from the GDP data set [*Lumpkin et al.*, 2012]. Here we set out a new method for binning and mapping the data that captures spatial and temporal variations in the data and

produces formal error bars for the mapped velocity components. These results are made available at http://www.aoml.noaa.gov/phod/dac/dac_meanvel.php¹.

2. Data and Methods

This analysis uses quality controlled data from the GDP from 1979 through June 2012, interpolated via kriging to regular 6-hour intervals [Hansen and Poulain, 1996]. Velocities every 6 hours are obtained via 12-hour centered differencing of the kriged positions. Recent analyses have found a significant fraction of the velocities in the time period 2002—2009 previously believed to be from drogued drifters were from undrogued drifters; in this study, only data from drogued drifters are used, following results of a manual reevaluation of drogue presence [Lumpkin *et al.*, 2012]. NCEP operational 6-hour surface (0.995 sigma level) winds W are interpolated to the drifter locations and a downwind slip of $7 \times 10^{-4} W$ [Niiler and Paduan, 1995] is removed from the remaining drifter velocities. The resulting velocities are lowpassed with a 2-point Butterworth filter with half-power cutoff at five days to remove tidal and near-inertial components of the flow, then decimated to daily values for this analysis. No attempt is made to separate Ekman and geostrophic velocities [e.g., Lumpkin and Garzoli, 2005]. Following Johnson [2001], zonal and meridional drifter speeds are mapped in elliptical bins centered on a $0.5^\circ \times 0.5^\circ$ longitude-latitude grid, with the ratio of semi-major to semi-minor axis and axis orientation set by the variance ellipse of eddy fluctuations

¹ Note to referees: this will be done pending publication; in the interim, the climatology is available at ftp://ftp.aoml.noaa.gov/phod/pub/lumpkin/greg/meandrift_world.mat. In this file, U, V, T contain the monthly climatology of currents and drifter-measured SST (dimensions: Lat \times Lon \times 12, 1) with associated error bars (Lat \times Lon \times 12, 2). Ubar (Lat \times Lon \times 11, 1) contains all 11 coefficients for the model fit Az to zonal speed, with associated error bars Ubar(Lat \times Lon \times 11, 2), and Vbar for meridional speed. Up2bar, Vp2bar and UpVpbar are $\langle u'^2 \rangle$, $\langle v'^2 \rangle$ and $\langle u'v' \rangle$, respectively.

(residuals with respect to the mapped current within the bin; see below) in the bin. For this study we chose bins with a set area of $\pi \times 2^\circ \text{ lat.} \times 2^\circ \text{ long.}$ Hence the bin area at $\pm 60^\circ$ latitude is half that at the equator, reflecting, albeit only weakly, the reduction of the Rossby radius of deformation at high latitudes [e.g., *Chelton et al.*, 1998], and its influence in reducing ocean current scales at higher latitudes [e.g., *Stammer et al.*, 2007]. The bin area is chosen subjectively to balance resolution of known current features while limiting aliased short-term variability in the maps. Other bin sizes were tested but found to be less optimal for global application: for example, bins half the size better resolved fine-scale currents in well-sampled regions of flow/topography interaction such as the Hawaiian Islands, but these small bins also tended to produce spurious features likely reflecting undersampled realizations of the time-varying mesoscale field in poorly-sampled regions. Alternatively, bins twice the size were superior for resolving large-scale currents in poorly-sampled regions, but overly smoothed features of the time-mean field (such as the Loop Current) that had converged at the resolution we chose. There are other possible choices for binning the data such as orienting bins along planetary potential vorticity contours [e.g., *Jacobsen et al.*, 2003] or the application of clustering methods to improve Lagrangian statistics [e.g., *Koszalka et al.* 2011]. Our choice is relatively simple, dynamically motivated, and homogenously applied around the globe, and results in a uniformly-gridded product.

Within each bin, the complex vector \mathbf{u} containing observations $u + iv$ of zonal u and meridional v drifter speed can be written $\mathbf{u} = \mathbf{A}\mathbf{z} + \mathbf{u}'$, where \mathbf{u}' are residuals (eddy fluctuations), \mathbf{z} is a vector containing 11 coefficients to be determined, and matrix \mathbf{A} describes the model used to map the large-scale currents:

$$A_j = [1 \quad SOI_j \quad \sin(2\pi t_j) \quad \cos(2\pi t_j) \quad \sin(4\pi t_j) \quad \cos(4\pi t_j) \quad x_j \quad x_j^2 \quad y_j \quad y_j^2 \quad x_j y_j]. \quad (1)$$

Here the subscript j indicates observation j collected at time t_j (in years). The unity term models the time mean. The term SOI_j is a running five-month average of the Southern Oscillation Index [Trenberth, 1984] centered at t_j ; this term models the influence of ENSO, and is especially important near the equator, where drifter observations may be biased towards El Niño-related periods of weak Trade Winds and associated low equatorial divergence [Johnson, 2001]. We include the SOI because it is generally well sampled over multiple cycles by the drifter data and is associated with strong variations in surface currents, especially across the tropical Pacific [e. g. Johnson et al., 2002]. The GDP-style drifters were deployed in their first decade of existence (1979-1989) almost solely in the tropical Pacific, motivated by the desire to resolve ENSO-related climate fluctuations. As noted by Johnson [2001], the SOI is correlated with the strength of Pacific equatorial divergence and thus surface drifter observational density, and can thus be expected to bias time-mean calculations if a SOI component is not included. We do not include other climate indices, such as the North Atlantic Oscillation [Hurrell, 1995], Pacific Decadal Oscillation [Mantua et al., 1997], or Antarctic Oscillation [Thompson and Wallace, 2000] because the data generally do not span all phases of these indices in as large a fraction of the bins, so they would not be well fit. However, as data records become longer, including such indices in future models might improve the results, which may be biased now towards one phase or the other of these phenomena. The sinusoidal terms fit annual and semi-annual harmonics [Johnson, 2001; Lumpkin, 2003]. The use of only two harmonics may not resolve the seasonal cycle fully everywhere, but it keeps the number of parameters in the model relatively low, and has been used previously and

successfully with sparsely sampled, inhomogenous oceanographic data sets [e.g.,
Ridgeway et al., 2002]. The final five terms in A_j model spatial gradients within the bin
 [Bauer et al., 1998; Johnson, 2001] and are expressed with respect to the non-
 dimensionalized zonal distance x_j and meridional distance y_j from the bin center,
 expressed in degrees longitude or latitude divided by 1° .

While a simultaneous fit to 11 coefficients is superior to a stepwise approach if all
 coefficients can be resolved by the data [c.f., *Lumpkin*, 2003], spurious results can result
 in bins with low observational density, particularly those that also have energetic
 mesoscale fluctuations. Examining results from the 11-coefficient fit as a function of
 observational density outside the tropical Pacific, we find that spuriously large results for
 the SOI coefficient are calculated in bins with < 365 drifter-days of observations
 (corresponding to 29 drifter-days per square degree). Comparable results are found for
 the seasonal sinusoid coefficients with < 90 drifter-days of observations. In bins with $<$
 365 drifter-days, the SOI term is not included in the model (1); in bins with < 90 drifter-
 days, the seasonal sinusoid terms are not included. If there are < 10 drifter-days of data
 (i.e., 2—3 Lagrangian integral time scales) then the calculation is not made and the bin is
 left blank.

The model is evaluated iteratively, starting with a circular bin, and calculating the
 resulting variance ellipses to determine a new ellipsoidal bin and new model coefficients
 [c.f., *Johnson*, 2001]. The calculation is iterated a total of five times for each bin to
 ensure convergence.

The Gauss-Markov estimator for \mathbf{z} in a given bin is

$$\mathbf{z} = \mathbf{R}_z \mathbf{A}^T (\mathbf{A} \mathbf{R}_z \mathbf{A}^T + \mathbf{R}_n)^{-1} \mathbf{u}, \quad (2)$$

144 [c.f., Wunsch, 1996; Lumpkin, 2003], where \mathbf{R}_z is the *a priori* (calculated before solving
 145 for \mathbf{z}) covariance matrix of the unknown coefficients in \mathbf{z} and \mathbf{R}_n is the variance structure
 146 of the eddy noise \mathbf{u}' . For this study each of the diagonal elements of \mathbf{R}_x are assumed to
 147 be equal to the squared range of \mathbf{u} and off-diagonal elements were set to zero. In
 148 principle prior knowledge could guide the values of the terms in \mathbf{R}_n ; our choice to set
 149 them all equal assumes that any term in (1) could potentially account for the observed
 150 variance of \mathbf{u} in each bin. Elements of \mathbf{R}_n are chosen to be

$$151 \quad R_n(\tau) = [\text{std}(u)^2 + i \text{std}(v)^2] \cos(\pi\tau / 2T_d) \exp[-(\pi\tau / 2\sqrt{2} T_d)^2] \quad (3)$$

152 following Lumpkin [2003], with $T_d = 10.33$ days, consistent with an integral eddy time
 153 scale of five days. This choice assigns degrees of freedom to the observations with the
 154 assumption that observations less than five days apart are not fully independent
 155 [Lumpkin, 2003], a conservative choice since many studies have found values of 2–3
 156 days for the integral time scale. The *a posteriori* error covariance matrix is

$$157 \quad \mathbf{P}_z = \mathbf{R}_z - \mathbf{R}_z \mathbf{A}^T (\mathbf{A} \mathbf{R}_z \mathbf{A}^T + \mathbf{R}_n)^{-1} \mathbf{A} \mathbf{R}_z \quad (4)$$

158 [c.f., Wunsch, 1996]. The square roots of the diagonal terms in \mathbf{P}_z are the formal error
 159 bars for the coefficients in \mathbf{z} ; for example, $[\mathbf{P}_z(1,1)]^{0.5}$ is the error for time-mean \mathbf{u} at the
 160 bin center. Since fitting multiple parameters at once can sometimes lead to spurious
 161 results, these error bars can be examined at any location to assess how well the various
 162 terms in the model are resolved. The total squared error for the mapped speed $\mathbf{A}\mathbf{z}$ is
 163 $\mathbf{A} \mathbf{P}_z \mathbf{A}^T$. This quantity can, for example, be used to derive error bars on seasonal or
 164 monthly mean values. The magnitudes of the coefficients \mathbf{z} and the residuals \mathbf{u}' are
 165 compared against the prior values (square roots of the diagonal terms in \mathbf{R}_z and \mathbf{R}_n ,

respectively) in each bin. The solution in a bin is rejected if $|z|$ exceeds the prior value in \mathbf{R}_z or if more than 40% of the residuals exceeds the prior value in \mathbf{R}_n .

The number of daily observations within each bin is highly inhomogeneous (Figure 1), being a function of deployment locations and the subsequent advection pathways, including regions of divergence and convergence that impact drifter residence times. Regions of poor data coverage (< 50 drifter days per square degree) are located in the southernmost Southern Ocean, the southeast Pacific Ocean west of Chile, the Southern Ocean south of Australia, the southwest Pacific immediately north of New Zealand, the western equatorial Indian Ocean, the central equatorial Atlantic Ocean, the easternmost Angola Basin, and the Java Sea (much of which is shallower than 15 m). The data are also not homogeneous in time: the earliest deployments (in 1979) were conducted solely in the tropical Pacific Ocean as part of the Tropical Ocean Global Atmosphere study [Niiler, 2001]. Sustained deployments began in the North Atlantic in 1989 [Fratantoni, 2001], the South Atlantic in 1993, the Indian Ocean in 1994, and the Tropical Atlantic in 1997 [Lumpkin and Garzoli, 2005]. From 1993–2002, the array averaged 500–700 drifters at any given time; it was increased to its current size of ~1250 drifters in late 2005 and has been subsequently sustained at approximately this size [Lumpkin and Pazos, 2007].

3. Results

We start with a presentation of the mean speed and streamlines as well as variance ellipses. We then discuss the regression of surface currents onto the SOI. Following that, we present the global seasonal cycle of the surface currents. As examples of the details

visible in the climatology, we discuss the seasonal cycle of surface currents in the western tropical Pacific Ocean and the surface divergence fields of the equatorial interior ocean basins. We conclude with a comparison to an oft-used surface current product.

3.1. Mean fields

Unsmoothed mean current speeds (to indicate local current magnitudes) with streamlines calculated from spatially smoothed velocities (to indicate large-scale interior current directions as well as qualitatively, the surface divergence field) clearly illustrate the prominent large-scale currents (Figure 2) such as the western boundary currents, their extensions, the equatorial current systems, and parts of the Antarctic Circumpolar Current (ACC). Only the streamlines are computed from smoothed fields, which do obliterate some smaller-scale regional features, with all other quantities displayed as mapped. The smoothing, applied only to bins with mean speeds $< 25 \text{ cm s}^{-1}$, is an average of the grid value and eight surrounding values, weighted by observational density, iterated 10 times to stress the large-scale field. The global histogram of unsmoothed mean speeds (Figure 2, inset) peaks at $4.5\text{--}6 \text{ cm s}^{-1}$, with 87% of the bins having a mean speed $< 25 \text{ cm s}^{-1}$ and 98% $< 50 \text{ cm s}^{-1}$.

3.1.1 Prominent currents

The structure of the Antarctic Circumpolar Current (ACC) is resolved as strong jets associated with the Southern Ocean fronts, surrounded by regions of relatively weak flow [Orsi *et al.*, 1995; Falco and Zambianci, 2011]. The ACC bifurcates east of the Drake Passage (Figure 2), with a significant portion flowing north in the western Atlantic

as the Malvinas Current, perhaps the equivalent of the western boundary for this otherwise zonally unbounded current [e.g., *Baker*, 1982]. After meeting the southward-flowing Brazil Current at the Brazil/Malvinas Confluence, the South Atlantic Current continues eastward across the South Atlantic and enters the southern Indian Ocean basin. Paralleling this to the south, the southern fronts of the ACC enters the Indian Ocean sector and slowly migrates southward as they flow eastward through the Indian and Pacific sectors [e.g., *Orsi et al.*, 1995; *Falco and Zambianci*, 2011], distinct at some longitudes, merged at others in this climatology. The ACC is narrower and in some areas up to 10 cm s^{-1} weaker than in previous mean current fields calculated from drifters prior to the recent drogue presence reassessment [*Lumpkin et al.*, 2013], and perhaps also affected by changes in mapping methods. The ACC is not resolved in the central and eastern South Pacific owing to the scarcity of drogued data in this region.

In the northern and equatorial Indian Ocean, with its strong seasonal cycle [e.g., *Schott and McCreary*, 2001], discussed below, the time-mean surface currents (Figure 2) are dominated by the northward-flowing Somali western boundary current and eastward equatorial Wyrтки Jet. In the Indian Ocean, the westward-flowing South Equatorial Current (SEC) at $24\text{--}6.5^\circ\text{S}$ is shifted further south than in the other oceans, with a maximum speed of $20\text{--}24 \text{ cm s}^{-1}$ at 12°S . The SEC is fed in part by the Indonesian Throughflow [*Gordon et al.*, 1997]. It bifurcates near 16°S upon reaching Madagascar, with the northern branch heading westward to Africa and then turning northward to join the East Africa Current [e.g., *Swallow et al.*, 1988]. The fate of the southern branch of the East Madagascar Current when it reaches the southern end of Madagascar is less clear [e.g., *Lutjeharms*, 2007], but in the mean drifter climatology it appears to form a jet

extending west-southwest from the southern tip of Madagascar to 28°S, 40°W. This jet then splits, with one branch flowing southward to join the Agulhas return current and the other flowing westward to join with the southward-flowing Mozambique Current to feed the Agulhas Current. The Agulhas has time-mean speeds of 60–150 cm s⁻¹, with the greatest speeds found from 32.5°S, 29°E to 34.5°S, 25.5°E. The Agulhas retroflects south of Africa, at 20–23°E in the mean — a bit further to the east than expected [e.g., *Lutjeharms*, 2007]— to feed the eastward-flowing South Indian Ocean Current which exhibits prominent meanders as it flows eastward to ~45°E and then east-southeastward to eventually merge with the ACC. On the east side of the Indian Ocean, the Leeuwin Current flows south along the west coast of Australia [*Feng et al.*, 2003], with a speed of 20–35 cm s⁻¹ in the latitude band 24–26.5°S, but it appears in the mean to be interrupted by an apparently permanent anti-cyclonic feature centered at ~29°S, 111°E; northward currents on the west side of this feature oppose the Leeuwin and reduce its strength. South of 30°S the Leeuwin exceeds 100 cm s⁻¹ in several bins. It wraps around the southwest corner of Australia and continues eastward along Australia’s south coast.

In the North Pacific, the Alaskan Stream [*Reed*, 1984] is apparent in the mean surface velocity from the drifter data (Figure 2) just south of Alaska and the Aleutian Island chain, petering out by about 170°E after it leaves its effective western boundary, near the dateline, where the island chain curves back to the northwest. The southward-flowing East Kamchatka and Oyashio, the western boundary currents of the subpolar gyre, are less prominent than the northward-flowing Kuroshio of the subtropical gyre, as is their eastward-flowing extension [e.g., *Qu et al.*, 2001] which slows to eastward speeds <10 cm s⁻¹ by 170°W.

258 The equatorial Pacific currents are prominent in the mean drifter velocities
 259 (Figure 2), with the westward flowing North Equatorial Current (NEC) at 9–24°N with a
 260 peak speed of 20 cm s⁻¹ at 11°N when averaged in the zonal band 150°E–140°W. The
 261 NEC extends from about 120°W to the Philippines, where it bifurcates to feed the
 262 northward-flowing Kuroshio and the southward flowing Mindanao Current [e.g., *Toole et*
 263 *al.*, 1990]. The Costa Rica Dome stands out as a small isolated anti-cyclonic circulation
 264 centered near 9°N, 95°W [*Fiedler*, 2002]. To the northwest, a region of anti-cyclonic
 265 circulation at 12–15°N, 105–95°W may be the rectified signature of the wind-generated
 266 anti-cyclonic Tehuantepec and Papagayo eddies which are generated in this region from
 267 October to July [*Palacios and Bograd*, 2005]; when the mean is recalculated using only
 268 August and September data (not shown), the eastward flow on the northern half of this
 269 region is not present. The North Equatorial Countercurrent (NECC) extends all the way
 270 across the Pacific [e.g., *Johnson et al.*, 2002]. In the Pacific the SEC is strongest at very
 271 low latitudes, with a narrow, ~45 cm s⁻¹ (averaged from 180–100°W) branch at 2°N and a
 272 larger branch of maximum speed 30–35 cm s⁻¹ centered at 4°S at 140–110°W that
 273 gradually shifts northward as it flows west, reaching 2°S by the dateline. These branches
 274 are separated by eastward surface flow at the equator in the central to eastern Pacific (the
 275 shoaled equatorial undercurrent) [*Johnson et al.*, 2002]. This feature is apparent in the
 276 unsmoothed maps, but absent in the streamlines, which are computed after smoothing the
 277 maps. The SEC is also strong along about 15°S from the dateline into the Coral Sea,
 278 where it bifurcates at the east coast of Australia, with part heading north towards the
 279 equator via the Solomon Sea (again, not visible in the smoothed streamlines) and the
 280 New Guinea Coastal Current and another portion feeding the southward flowing East

Australia Current [e.g., *Ganachaud et al.*, 2008] which has a peak speed of 90 cm s^{-1} at 30.5°S , 153.5°E .

In the subpolar North Atlantic Ocean, the $30\text{--}35 \text{ cm s}^{-1}$ East Greenland Current rounds Cape Farewell (Fig. 2; visible in the current speeds) to become the west Greenland current with peak speeds of $45\text{--}50 \text{ cm s}^{-1}$, and then the $15\text{--}30 \text{ cm s}^{-1}$ Labrador Current, before meeting the Gulf Stream extension near Newfoundland [e.g., *Higginson et al.*, 2011]. The northward-flowing Norwegian Atlantic Current is also prominent in the drifter data [e.g., *Jakobsen et al.*, 2003; *Koszalka et al.*, 2011]. The return currents in the gyre interior are discussed below.

In the southwestern tropical Atlantic, the North Brazil Current [*Garzoli et al.*, 2004; *Lumpkin and Garzoli*, 2005] bifurcates, with the western portion, the Guyana Current [c.f., *Richardson and Walsh* 1986], entering the Caribbean to form the $30\text{--}50 \text{ cm s}^{-1}$ Caribbean Current, which passes north of a clearly defined (Figure 2; visible in the current speeds) Columbia-Panama gyre in the southern Columbia Basin [c.f., *Richardson*, 2005]. The Caribbean Current feeds into the Yucatan Current, which in turn feeds the high-speed Loop Current in the Gulf of Mexico [c.f., *Molinari and Morrison*, 1988], which in turn joins the Gulf Stream flowing north to Cape Hatteras. In the time-mean the Gulf Stream is $70\text{--}80 \text{ cm s}^{-1}$, with speeds exceeding 90 cm s^{-1} in the Florida Current and at its separation from the coast near Cape Hatteras. The Gulf Stream splits to the northeast to feed the North Atlantic Current [e.g., *Schmitz and McCartney*, 1993] and to the southeast to return to the subtropical Gyre. The North Atlantic Current in turn splits to feed the North Atlantic Drift that returns to the subpolar gyre, and the Azores Current

[e.g., *Klein and Siedler*, 1989] that eventually feeds the equatorward eastern boundary flow and upwelling regime associated with the Canary Current [e.g., *Mason et al.*, 2012].

The tropical Atlantic mean circulation (Figure 2) is dominated by a zonally elongated clockwise gyre consisting of the westward northern and central branches of the SEC, the northwestward North Brazil Current (NBC) and its southeastward retroflection, and the eastward NECC and Guinea Current [*Lumpkin and Garzoli*, 2005]. Very large time-mean speeds of 80–140 cm s⁻¹ are found in the NBC, with the largest speeds located at 4–7°N, 54–50°W immediately before the NBC splits into the southeastward Retroflection and the westward Guyana Current. Upwelling and cross-equatorial flow of surface waters evident in the mean surface drifter climatology play a role in the warm return flow of the Atlantic Meridional Overturning Circulation [e.g., *Roemmich*, 1981].

In the South Atlantic, the surface expression of the southern SEC (Figure 2) bifurcates against the South American coast at 14–14.5°S to form the north-northeastward NBC and the south-southwestward Brazil Current, consistent with the literature [e.g., *Rodrigues et al.*, 1999]. The Brazil Current meets the north-northeastward Malvinas Current at 37°S, 54°W in the time-mean at the surface. The Brazil-Malvinas Confluence is a complex, energetic region [e.g., *Provost et al.*, 1992, *Lumpkin and Garzoli*, 2011]; in the mean drifter climatology the Malvinas Current has speeds of 30–50 cm s⁻¹ against the South American shelf, with comparable speeds in the southward Brazil/Malvinas Confluence jet which extends south to about 45°S. The eastward flow emerging from the Confluence region is strongest at 48°S, associated with the Subpolar Front, with a secondary jet at 40°S associated with the Subtropical Front [*Orsi et al.*, 1995].

3.1.2 Interior gyres, convergence, and divergence.

Global streamlines converge in the centers of the subtropical gyres, associated with the convergent subtropical fronts (Figure 2). These fronts terminate in so-called garbage patches in the both hemispheres of the eastern (centered near 35°N, 140°W and 30°S, 100°W) Pacific and the eastern (25°S, 100°E) South Indian oceans [Maximenko *et al.*, 2012; van Sebille *et al.*, 2012]. In the Atlantic the convergences are centered further to the west (near 30°N, 50°W and 30°S, 25°W) [e.g., Law *et al.*, 2011]. In contrast, streamlines diverge from the subpolar gyres of the North Pacific and North Atlantic. Subpolar divergence south of the ACC, where deep water is upwelled [e.g., Sloyan and Rintoul, 2001], is not resolved by the drifters.

Divergence from the equatorial Pacific and Atlantic is also extremely prominent (Figure 2), and is associated with the cold tongues of upwelled water from below [e.g., Johnson *et al.*, 2001; Grodsky and Carton, 2002]. However, in the equatorial Indian Ocean, acceleration of the flow across the equator is consistent with weaker horizontal divergence (see Section 3.3) that is not as visually apparent as in the equatorial Pacific and Atlantic. In fact, there is a net southward surface flow observed at the equator, closing a mean cell of subducted water in the Southern Hemisphere and upwelled water in the North [Schott *et al.*, 2004]. Divergence is apparent near 8°S in the western tropical Indian Ocean, where the winds bring the thermocline close to the surface [e.g., Hermes and Reason, 2008], as well as in the Costa Rica Dome near 9°N, 90°W [Fiedler, 2002].

Streamlines also clearly diverge from the west coasts of North and South America and Africa (apart from the latitude band of the NECC, Figure 2), where the equatorward-

flowing eastern boundary currents are associated with coastal upwelling [e.g., *Bograd et al.*, 2009; *Colas et al.*, 2012; *Hutchings et al.*, 2009; *Nyckær and Van Camp*, 1994]. In contrast, the streamlines do not indicate divergence along the Australian west coast, where the poleward-flowing Leeuwin Current (visible in the current speeds) carries warm water southward, and the winds and circulation inhibit upwelling [*Feng et al.*, 2003].

3.2 Variance

The mean speed of eddy fluctuations with respect to the model fit (i.e., fluctuations with respect to the time-mean, seasonal, and SOI-related variations, equal to the square root of twice the eddy kinetic energy) shows large geographic variations (Figure 3). These results are comparable to those from satellite altimetry [e.g., *Ducet et al.*, 2000], except that the surface drifter analysis can be carried to the equator as geostrophy need not be assumed. Maximum eddy speeds exceeding 70 cm s^{-1} are found in the Somali Current region; values $> 60 \text{ cm s}^{-1}$ are also found in the Gulf Stream and Agulhas Retroflection, and $> 50 \text{ cm s}^{-1}$ also in the Loop Current, Florida Current, the Pacific NECC and northern SEC at $115\text{--}130^\circ\text{W}$ (presumably associated with energetic Tropical Instability Waves), Kuroshio Current, Brazil/Malvinas Confluence, Agulhas Return Current, North Brazil Current Retroflection, Mozambique Channel, and the East Australian Current. Enhanced eddy energy is also seen along the path of the ACC, west of the Hawaiian Islands, in the Pacific Subtropical Countercurrents, and along much of the NECCs of the Atlantic and Pacific basins.

In contrast, “eddy deserts” with time-mean eddy speeds $< 10 \text{ cm s}^{-1}$ dominate three large regions: the subtropical South Atlantic, the subpolar North Pacific, and the

southeastern South Pacific ($\sim 110\text{--}85^\circ\text{W}$ from $40\text{--}10^\circ\text{S}$, and extending west to 170°W in the band $45\text{--}35^\circ\text{S}$). Much smaller eddy deserts are found in the central subtropical North Atlantic, west and south of New Zealand and south of the merged Agulhas Return Current and ACC immediately south of Kerguelen Island. Again, drifter speeds in this study have been lowpass filtered at 5 days; higher frequency motion may be present in these eddy deserts [Griffa *et al.*, 2008].

The variance ellipses for these eddy fluctuations (Figure 3) tend to align with most of the major currents such as the Gulf Stream and Kuroshio, although this tendency is less apparent in the East Australia and the Agulhas Return currents. Near the coasts, the ellipses tend to align with the coastlines. In the ocean interiors they are generally more circular, except at low latitudes, particularly in the Pacific and Indian equatorial bands, where they are zonally elongated. The coastal and equatorial waveguides are presumably largely responsible for these patterns.

3.3 Southern Oscillation Index (SOI) and surface currents

Current speeds and directions from the regression against the SOI (Figure 4, plotted for $\text{SOI} = -1$, corresponding to a moderate El Niño) contain the anticipated eastward (and slightly equatorially convergent) surge of surface currents in the Equatorial Pacific [e.g., Johnson *et al.*, 2000]. Eastward values of $10\text{--}20\text{ cm s}^{-1}$ are seen in the equatorial Pacific ($2^\circ\text{S}\text{--}3^\circ\text{N}$) from 160°E to nearly 160°W , and along $155\text{--}110^\circ\text{W}$ from $2\text{--}3^\circ\text{N}$. A weaker response mirroring the $2\text{--}3^\circ\text{N}$ response is seen just south of the equator in the eastern tropical Pacific. East of 145°W , the response on the equator is not statistically significantly different from zero due to the scarcity of observations (Figure

1). In the western tropical South Pacific there is another patch of anomalous westward flow associated with an El Niño-related shift in the South Pacific Convergence Zone [e.g., *Cai et al.*, 2012]. Curiously, the response in the Tehuantepec and Papagayo eddy region 12–15°N, 105–95°W suggests a weakening of the anti-cyclonic recirculation even though more frequent and stronger anti-cyclonic eddies are thought to be generated there during El Niños [*Palacios and Bograd*, 2005].

In the Indian Ocean, El Niño-related westward speeds of ~4–8 cm s⁻¹ can be found in a band stretching west-northwestward across the basin from ~12°S, 100°E to ~1°N, 50°E, generally increasing toward the west. There is another patch of westward flow just north of the equator south of India and Sri Lanka associated with El Niño. Strong (15–25 cm s⁻¹) southwestward anomalies against Somalia oppose the seasonal northeastward Somali Current north of 4°N during El Niño; SOI-related variations further south cannot be resolved due to observational densities of < 365 drifter days per bin. The large spatial extent and coherent directions in the features associated with El Niño discussed above suggest they may be robust. Other less spatially coherent patterns include a slowing of the surface currents in the Gulf Stream, eastward flow in the deep section of the eastern Bering Sea, and westward flow in the Mediterranean Sea, all apparently during El Niño. However, these latter features, given their relatively small spatial extent and absence of documented teleconnection mechanisms, may simply result from spurious correlations with the SOI. There are isolated patches of response in other areas, but nothing aside from the patterns already discussed stands out as spatially coherent.

3.4. Seasonal variations

Monthly mean ocean currents for climatological February, August, May, and November (Figures 5–6) illustrate the seasonal cycle of global surface currents. For example, the eastward Wyrtki jet in the equatorial Indian Ocean is prominent in May ($\sim 50 \text{ cm s}^{-1}$) and November ($\sim 70 \text{ cm s}^{-1}$) while being absent in August and reversed in February [e.g., Nagura and McPhaden, 2010]. Likewise the Somali Current is completely spun-up in August during the Southwest Monsoon, but reversed in February near the end of the Northeast Monsoon [e.g., Schott *et al.*, 1990]. The Bay of Bengal shows a strong seasonal cycle as well, with current directions reversing completely [e.g., Shenoi *et al.*, 1999]. Interior flow across the equator is largely southward in August, and northward in February, with seasonally reversing surface winds driving a shallow “cross-equatorial roll” with subsurface flow opposite the surface flow [e.g., Schott *et al.*, 2002]. Further to the south, the surface expression of the South Equatorial Current is substantially weaker in August than in other seasons.

The seasonality of the NECC is clearly seen in the Pacific and Atlantic basins, revealing for example an intense Atlantic NECC emerging from the North Brazil Current Retroflection in August while neither exists in May [e.g., Lumpkin and Garzoli, 2005]. The Pacific NECC is quite strong in August and November, but much weaker in February and May [e.g., Johnson *et al.*, 2002]. The South Equatorial Countercurrent in the western Pacific Ocean at $11\text{--}8^\circ\text{S}$ is clearly seen in February (and also in December, January and March, not shown) while being absent in other months [Chen and Qiu, 2004].

The gyre-scale circulations (Figures 5–6, streamlines) also exhibit seasonal migrations, which are no doubt associated with seasonal wind shifts [vis., *Risien and Chelton*, 2008]. For example, the centers of the northern hemisphere subtropical gyres shift to the south in February and to the north in August. In the North Pacific Ocean there is a dramatic shift in the latitude of the interior recirculation gyre, from $\sim 20^{\circ}\text{N}$ in February to $\sim 40^{\circ}\text{N}$ in August. This seasonal migration may have a significant modulating impact on the convergence of floating material in the “garbage patch” of the North Pacific, compared to calculations based on time-mean Lagrangian displacement statistics [e.g., *Maximeko et al.*, 2012] in which these shifts would spuriously increase the inferred time-mean lateral diffusivity.

3.4.1 Tropical west Pacific surface currents

Many fine-scale details of the surface circulation are difficult to see when plotted at the global scale, but are resolved by the drifter observations in the climatology presented here. For example, in the western Pacific (Figure 7) the southward-flowing Mindanao Current can be seen to split immediately north of the northeastern tip of the Celebes year-round, with the westward branch entering the Celebes Sea, and the eastward branch feeding the NECC; the cyclonic Mindanao Eddy is located between the Mindanao Current and NECC throughout the year [c.f., *Arruda and Nof*, 2003]. In Boreal winter, the strongly zonal NECC separates into its main branch running along $\sim 5^{\circ}\text{N}$ and a secondary branch flowing ESE along the northwestern New Guinea coast (Figure 7). This branch reverses through Boreal spring, and by August the WNW New Guinea Coastal Current (NGCC) has surfaced. At the confluence of the Mindanao Current’s

eastward branch and the NGCC, a narrow northeastward-flowing jet develops, the eastern side of which recirculates to form the Halmahera Eddy [c.f., *Arruda and Nof*, 2003] which is not present in Boreal winter but is clearly visible in Boreal summer through fall. This eddy is thought to play a significant role in modulating exchange between the Pacific and Indian basins through the Indonesian Throughflow [*Qu et al.*, 1999].

3.4.2. Interior equatorial surface divergence

The seasonal divergence in the equatorial interior of the three ocean basins (Figure 8) contrast strongly. Equatorial divergence in the Indian Ocean peaks in August with the relaxation of the Wyrtki Jet; the flow is strongly convergent in November through January. An off-equatorial divergence is evident in the South Indian Ocean, centered near 8°S in December–April, and closer to 5°S in May–August. This feature may be associated with the thermocline ridge near that latitude in the South Indian Ocean [e.g., *Hermes and Reason*, 2008]. In contrast, equatorial divergence is present year-round in the central Pacific and Atlantic basins [e.g., *Hansen and Paul*, 1987; *Johnson et al.*, 2001; *Grodsky and Carton*, 2002], although the magnitude displays a seasonal modulation in both basins with stronger divergence in Boreal spring vs. Boreal fall (mirroring the development of the cold tongue in the eastern regions of these basins). Off-equatorial convergence is seen throughout the year in the central Pacific south of the equator, but is more seasonally modulated to the north with a convergence maximum at 4–5°N in May–June. In the central Atlantic, convergent maxima are seen at 4–8° N during May–August, and at 6–4°S during June–September. These patterns of equatorial

divergence and off-equatorial convergence are associated with the shallow tropical overturning cells in these basins [e.g., *Perez et al.*, 2010].

4. Summary and Discussion

We use a global set of drogued drifter velocity measurements to map the time-mean, seasonal, and SOI-related components of near-surface currents at high resolution. Our approach combines aspects of three previous mapping efforts [*Bauer et al.*, 1998; *Johnson*, 2001; *Lumpkin*, 2003] to address spatial and temporal variations in the data and to produce formal error bars for the various components (mean, seasonal cycle, and SOI regression) of the currents. Our analysis also takes advantage of data set corrections from a recent reevaluation of drogue presence [*Lumpkin et al.*, 2013], one result of which is significantly reduced speeds for currents such as the ACC. However, it is possible that downwind (and down-wave) slip, which has not been directly measured for drogued drifters at wind speeds $>10 \text{ m s}^{-1}$ [*Niiler et al.*, 1995], may exceed the linear slip removed in the recent data set update by Lumpkin et al. [2013], and as such there may still be downwind bias in regions of strong winds.

Assuming a mean density of 1025 kg m^{-3} , the global distribution of total kinetic energy (Figure 9d) amounts to a total of $4.6 \times 10^{17} \text{ J}$ in the upper 30 m, in all bins with more than 10 drifter days of data (for reference, the global total variable kinetic energy of the full-depth ocean is estimated at $3.8 \times 10^{18} \text{ J}$ [*Wunsch*, 1998]). Our estimate does not include energy at Lagrangian periods shorter than five days including inertial, tidal, submesoscale, and high-frequency mesoscale motions. Mean currents contribute a substantial fraction to the total kinetic energy (Figure 9a) where one would expect: in the

western boundary currents and their extensions, in the North Equatorial currents and the North Equatorial countercurrents of the Atlantic and Pacific oceans, and in segments of the Antarctic Circumpolar Current. These are all locations where the total kinetic energy is high (Figure 9d), and – except for the equatorial currents and regions of the ACC – where there is topographic confinement. However, the mean currents also constitute a substantial fraction of the total kinetic energy in the South Equatorial currents of all three oceans as well as in the interior of the subpolar North Pacific gyre, all eddy desert regions (with the exception of the Indian Ocean SEC) where the total kinetic energy is relatively low. Globally, the mean currents contribute 1.6×10^{17} J of kinetic energy in the upper 30 m, 36% of the total estimated KE in bins with > 10 drifter days of observations.

The seasonal contribution (Figure 9c) to the total kinetic energy (Figure 9d) is 20–40% in the Pacific and Atlantic North Equatorial countercurrents. It is substantial throughout much of the Indian Ocean north of about 10°S, with maxima of 50–70% at 0–5°N, 55–70°E. Another location of strong seasonal contribution is the eastern tropical South Atlantic Ocean, just west of Africa: it contributes 20–30% of the total KE throughout the Angola Basin, and 40–70% against the African coast. Seasonal variations represent a global total of 6.7×10^{16} J of kinetic energy in the upper 30 m in all bins with > 90 drifter days of observations, 15% of the total KE in those bins.

The fractional contribution of SOI-related variations (not shown) is generally small, exceeding 10% only in the vicinity of the equator from 165°E to 165°W. It represents a global total of 2.6×10^{15} J of kinetic energy in the upper 30 m in all bins with > 365 drifter days of observations, 1% of the total in those bins.

530 The eddy contribution (Figure 9b) to the total kinetic energy (Figure 10d)
531 dominates much of the ocean, especially the interior of the subtropical gyres and the
532 subpolar North Atlantic Gyre. The fraction of the total kinetic energy accounted for by
533 eddies with Lagrangian periods > 5 days exceeds 50% in 69% of bins with > 10 drifter
534 days of observations. However, in much of this area the total kinetic energy is small.
535 EKE dominates in the well-known eddy regions such as the Gulf Stream and Kuroshio
536 recirculation gyres, Agulhas and North Brazil Current ring pathways, and the
537 Brazil/Malvinas Confluence. Eddies also make a large contribution between the North
538 Equatorial currents and the various branches of the South Equatorial currents, where
539 tropical instability waves [e.g., *Chelton et al.*, 1999] are energetic. The eddy deserts of
540 the eastern North Pacific, eastern South Atlantic, and eastern South Pacific each have
541 portions where mean currents are dominant, but also portions where the eddies are
542 dominant, with low total energy levels throughout. The EKE represents a total of $2.4 \times$
543 10^{17} J of kinetic energy in the upper 30 m in all bins with > 10 drifter days of
544 observations, 49% of the total KE in those bins. As noted above, eddy energy at periods
545 smaller than five days is not included in this value.

546 The time-mean and seasonal currents derived here can be used for purposes such
547 as model validation and product evaluation. For example, there are large and spatially
548 coherent differences (Figure 10a) between the mean velocity in the drifter climatology
549 and the January 1993–December 2003 mean velocity from the $1/3^\circ$ unfiltered satellite-
550 derived Ocean Surface Current Analysis Real-time (OSCAR) product [*Bonjean and*
551 *Lagerloef*, 2002] including geostrophic, Ekman, and buoyancy components. While inter-
552 annual variations may play a role in some of the discrepancies, the drifter climatology is

faster by up to 20–25 cm s⁻¹ in the Gulf Stream and Kuroshio currents, and up to 35 cm s⁻¹ faster in segments of the ACC and Agulhas Return Current. Along the northern branch of the South Equatorial Current at 1–3°N in the Pacific, the drifter climatology is 20–50 cm s⁻¹ faster to the west than in the OSCAR product; on the equator in the Atlantic it is 20–35 cm s⁻¹ faster to the west (Figure 10). These dramatic differences may be due both to smoothing and difficulties in calculating the near-equatorial quasi-geostrophic flow for OSCAR.

Differences between this new drifter-derived climatology and products giving time-mean geostrophic speed (such as the CNES-CLS09 MDT product [Rio *et al.* 2011], Figure 10b) can be used to infer the ageostrophic component of drifter motion. Although it extends beyond the scope of this study, it would be interesting to remove the ageostrophic motion, recalculate the distribution of variance about the time-mean speeds, and compare the results to eddy kinetic energy from altimetry [c.f., Fratantoni, 2001]. Because the drifter climatology gives total near-surface currents, it can also be used to improve our estimates of wind stress and turbulent heat fluxes, which depend on the relative speed of the wind over the moving ocean surface [Fairall *et al.*, 2003]. Ocean currents have been demonstrated to affect the wind stress field and its curl and divergence [Kelly *et al.*, 2001; Risien and Chelton, 2008].

Our results include formal error bars for all coefficients in the model (1). These error bars (Figure 11) demonstrate where currents are well-resolved by the data, and conversely where more data are needed. Absolute error estimates (Figure 11, left panels) are generally large where the signals are large (Figures 2, 4) and where observations are sparse (Figure 1). The signal-to-noise ratio for the time-mean current speed (Figure 11b)

is small in areas with weak time-mean currents such as the centers of the subtropical gyres. Elsewhere, this ratio indicates that time-mean currents are well-resolved away from seasonally ice-covered regions except in four areas: (1) the ACC in the central and eastern South Pacific; (2) the southwestern and northwestern Gulf of Mexico, west of 90°W excluding the well-resolved Loop Current pathway; (3) the Indonesian Sea, which is relatively shallow and undersampled by drifters (Figure 1); and (4) the Coral Sea. Seasonal variations are well-resolved throughout the tropical Pacific, along the path of the NECC in the central and western tropical Atlantic, and off the equator in the tropical Indian basins. Seasonal variations are more marginally resolved in the Gulf of Guinea and southern tropical Atlantic and equatorial Indian oceans (Figure 11d), where observations are more sparse (Figure 1). Time-mean and seasonal error estimates are large in regions of seasonal or near-permanent ice coverage. The SOI-related coefficient is well-resolved in the central and western tropical Pacific and across the central and eastern tropical Indian basins, but (as noted earlier) is not well resolved by the data on the equator east of 145°W owing to sparse observational density.

The climatology of time-mean and seasonal currents derived in this study, along with the model coefficients and associated errors, is available at http://www.aoml.noaa.gov/phod/dac/dac_meanvel.php. Animations of these currents in various regions are available at http://www.aoml.noaa.gov/phod/dac/dac_animations.php.

Acknowledgments. NOAA Research and the NOAA Climate Program Office funded this work. RL received additional support from the Atlantic Oceanographic and Meteorological Laboratory. Conversations and input from Chris Meinen, Carlisle Thacker, Kathleen Dohan, and three anonymous reviewers helped improve the original manuscript. The drifter data were collected and made freely available by the Global Drifter Program (<http://www.aoml.noaa.gov/envids/gld/index.php>). OSCAR data are available at <http://www.oscar.noaa.gov>. PMEL publication 3902.

References

- Arruda, W. Z. and D. Nof (2003), The Mindanao and Halmahera Eddies—Twin Eddies Induced by Nonlinearities, *J. Phys. Oceanogr.*, *33*, 2815–2830.
- Baker, D. J. (1982), A note on Sverdrup balance in the Southern Ocean, *J. Mar. Res.*, *40*, (Suppl.), S21–S26.
- Bauer, S., M. S. Swenson, A. Griffa, A. J. Mariano, and K. Owens (1998), Eddy–mean flow decomposition and eddy-diffusivity estimates in the tropical Pacific Ocean. 1. Methodology, *J. Geophys. Res.*, *103*(C13), 30,855–30,871, doi:10.1029/1998JC900009.
- Bograd, S. J., I. Schroeder, N. Sarkar, X. Qiu, W. J. Sydeman, and F. B. Schwing (2009), Phenology of coastal upwelling in the California Current, *Geophys. Res. Lett.*, *36*, L01602, doi:10.1029/2008GL035933.
- Bonjean, F. and G. S. Lagerloef (2002). Diagnostic Model and Analysis of the Surface Currents in the Tropical Pacific Ocean, *J. Phys. Oceanogr.*, *32*, 2938–2954.
- Cai, W., and co-authors (2012), More extreme swings of the South Pacific convergence zone due to greenhouse warming, *Nature*, *488*, 365–369, doi:10.1038/nature11358.
- Chelton, D. B., R. A. deSzoek, M. G. Schlax, K. El Naggar, and N. Siwertz (1998), Geographical variability of the first baroclinic Rossby radius of deformation, *J. Phys. Oceanogr.*, *28*, 433–460. doi: [http://dx.doi.org/10.1175/1520-0485\(1998\)028<0433:GVOTFB>2.0.CO;2](http://dx.doi.org/10.1175/1520-0485(1998)028<0433:GVOTFB>2.0.CO;2).
- Chelton, D. B., F. J. Wentz, C. L. Gentemann, R. A. de Szoek, and M. G. Schlax (2000), Satellite microwave SST observations of transequatorial tropical instability waves, *Geophys. Res. Lett.*, *27*, 1239–1242, doi:10.1029/1999GL011047.

625 Chen, S., and B. Qiu (2004), Seasonal variability of the South Equatorial Countercurrent,
626 *J. Geophys. Res.*, *109*, C08003, doi:10.1029/2003JC002243.

627 Colas, F., J. C. McWilliams, X. Capet and J. Kurian (2012), Heat balance and eddies in
628 the Peru-Chile current system, *Climate Dynamics*, *39*, 509–529, doi: 10.1007/s00382-
629 011-1170-6.

630 Davidson, F. J. M., A. Allen, G. B. Brassington, Ø. Breivik, P. Daniel, M. Kamachi, S.
631 Sato, B. King, F. Lefevre, M. Sutton, and H. Kaneko (2009), Applications of GODAE
632 ocean current forecasts to search and rescue and ship routing, *Oceanogr.* *22*(3):176–
633 181, <http://dx.doi.org/10.5670/oceanog.2009.76>.

634 Ducet, N., P.-Y. Le Traon, and G. Reverdin (2000), Global high-resolution mapping of
635 ocean circulation from TOPEX/Poseidon and ERS-1 and -2, *J. Geophys. Res.*, *105*,
636 19,477–19,498, doi:10.1029/2000JC900063.

637 Fairall, C.W., Bradley, E.F., Hare, J.E., Grachev, A.A., and Edson, J.B. (2003), Bulk
638 parameterization of air-sea fluxes: Updates and verification for the COARE
639 algorithm, *J. Climate*, *16*, 571–591.

640 Falco, P., and E. Zambianchi (2011), Near-surface structure of the Antarctic Circumpolar
641 Current derived from World Ocean Circulation Experiment drifter data, *J. Geophys.*
642 *Res.*, *116*, C05003, doi:10.1029/2010JC006349.

643 Feng, M., G. Meyers, A. Pearce, and S. Wijffels (2003), Annual and interannual
644 variations of the Leeuwin Current at 32°S, *J. Geophys. Res.*, *108*, 3355,
645 doi:10.1029/2002JC001763.

646 Fiedler, P. C. (2002), The annual cycle and biological effects of the Costa Rica Dome.
647 *Deep-Sea Res. II*, 49, 321–338, doi: 10.1016/S0967-0637(01)00057-7.

648 Fratantoni, D. M. (2001), North Atlantic surface circulation during the 1990's observed
649 with satellite-tracked drifters, *J. Geophys. Res.-Oceans*, 106 (C10), 22,067–22,093.

650 Ganachaud, A., L. Gourdeau, and W. Kessler (2008), Bifurcation of the subtropical South
651 Equatorial Current against New Caledonia in December 2004 from a hydrographic
652 inverse box model, *J. Phys. Oceanogr.*, 38, 2072–2084, doi:10.1175/2008JPO3901.1.

653 Garzoli, S. L., A. Ffield, W. E. Johns, and Q. Yao (2004), North Brazil Current
654 retroflection and transports, *J. Geophys. Res.*, 109, C01013,
655 doi:10.1029/2003JC001775.

656 Gordon, A. L., S. Ma, D. B. Olson, P. Hacker, A. Ffield, L. D. Talley, D. Wilson, and M.
657 Baringer (1997), Advection and diffusion of Indonesian Throughflow Water within
658 the Indian Ocean South Equatorial Current, *Geophys. Res. Lett.*, 24, 2573–2576,
659 doi:10.1029/97GL01061.

660 Griffa, A., R. Lumpkin, and M. Veneziani (2008), Cyclonic and anticyclonic motion in
661 the upper ocean, *Geophys. Res. Lett.*, 35, L01608, doi:10.1029/2007GL032100.

662 Grodsky, S. A. and J. A. Carton (2002), Surface drifter pathways originating in the
663 equatorial Atlantic cold tongue, *Geophys. Res. Lett.*, 29, 2147,
664 doi:10.1029/2002GL015788.

665 Grodsky, S. A., R. Lumpkin, and J. A. Carton (2011), Spurious trends in global surface
666 drifter currents, *Geophys. Res. Lett.*, 38, L10606, doi:10.1029/2011GL047393.

667 Hansen, D. V., and C. A. Paul (1987), Vertical motion in the eastern equatorial Pacific
668 inferred from drifting buoys. *Oceanol. Acta*, 6, 27–32.

669 Hansen, D., and P.-M. Poulain (1996), Quality control and interpolations of WOCE-
 670 TOGA drifter data, *J. Atmos. Oceanic Technol.*, *13*, 900–909.

671 Hermes, J. C., and C. J. C. Reason (2008), Annual cycle of the South Indian Ocean
 672 (Seychelles-Chagos) thermocline ridge in a regional ocean model, *J. Geophys. Res.*,
 673 *113*, C04035, doi:10.1029/2007JC004363.

674 Higginson, S., K. R. Thompson, J. Huang, M. Véronneau, and D. G. Wright (2011), The
 675 mean surface circulation of the North Atlantic subpolar gyre: A comparison of
 676 estimates derived from new gravity and oceanographic measurements, *J. Geophys.*
 677 *Res.*, *116*, C08016, doi:10.1029/2010JC006877.

678 Hurrell, J.W. (1995), Decadal trends in the North Atlantic Oscillation: Regional
 679 temperatures and precipitation, *Science*, *269*, 676–679.

680 Hutchings, L., and co-authors (2009), The Benguela Current: An ecosystem of four
 681 components, *Prog. Oceanogr.*, *83*, 15–32, doi:10.1016/j.pocean.2009.07.046.

682 Jakobsen, P. K., M. H. Ribergaard, D. Quadfasel, T. Schmith, and C. W. Hughes (2003),
 683 Near-surface circulation in the northern North Atlantic as inferred from Lagrangian
 684 drifters: Variability from the mesoscale to interannual, *J. Geophys. Res.*, *108*(C8),
 685 3251, doi:10.1029/2002JC001554.

686 Johnson, G. C. (2001), The Pacific Ocean subtropical cell surface limb. *Geophys. Res.*
 687 *Lett.*, *28*, 1771–1774, doi:10.1029/2000GL012723.

688 Johnson, G. C., M. J. McPhaden, and E. Firing (2001), Equatorial Pacific Ocean
 689 horizontal velocity, divergence, and upwelling. *J. Phys. Oceanogr.*, **31**, 839–849,
 690 doi:10.1175/1520-0485(2001)031<0839:EPOHVD>2.0.CO;2.

691 Johnson, G. C., M. J. McPhaden, G. D. Rowe, and K. E. McTaggart (2000). Upper

692 equatorial Pacific Ocean current and salinity variability during the 1996–1998 El
 693 Niño–La Niña cycle. *J. Geophys. Res.*, *105*, 1037–1053, doi:10.1029/1999JC900280.
 694 Johnson, G. C., B. M. Sloyan, W. S. Kessler, and K. E. McTaggart (2002), Direct
 695 measurements of upper ocean currents and water properties across the tropical Pacific
 696 Ocean during the 1990's, *Progress in Oceanography*, *52*, 31–61, doi:10.1016/S0079-
 697 6611(02)00021-6.
 698 Kelly, K. A., S. Dickinson, M. J. McPhaden, and G. C. Johnson (2001), Ocean currents
 699 evident in satellite wind data, *Geophysical Research Letters*, *28*, 2469–2472,
 700 doi:10.1029/2000GL012610.
 701 Klein, B., and G. Siedler (1989), On the origin of the Azores Current, *J. Geophys. Res.*,
 702 *94*, 6159–6168, doi:10.1029/JC094iC05p06159.
 703 Koszalka, I, J. H. LaCasce, M. Andersson, K. A. Orvikb, and C. Mauritzen (2011),
 704 Surface circulation in the Nordic Seas from clustered drifters, *Deep-Sea Res. I*, *58*,
 705 468–485, doi:10.1016/j.dsr.2011.01.007.
 706 Law, K. L., S. Morét-Ferguson, N. A. Maximenko, G. Proskurowski, E. E. Peacock, J.
 707 Hafner, and C. M. Reddy (2010), Plastic Accumulation in the North Atlantic
 708 Subtropical Gyre, *Science*, *329*, 1185–1188, doi:10.1126/science.1192321.
 709 Lumpkin, R. (2003), Decomposition of surface drifter observations in the Atlantic
 710 Ocean, *Geophys. Res. Lett.*, *30* (14), 1753, doi:10.1029/2003GL017519.
 711 Lumpkin, R. and S. Garzoli (2005), Near-surface circulation in the Tropical Atlantic
 712 Ocean, *Deep-Sea Res. I*, *52*, 495–518.
 713 Lumpkin, R., and M. Pazos (2007), Measuring surface currents with Surface Velocity
 714 Program drifters: the instrument, its data and some recent results, in Lagrangian

Analysis and Prediction of Coastal and Ocean Dynamics, edited by A. Griffa, A. D. Kirwan, A. Mariano, T. Özgökmen, and T. Rossby, chap. 2, pp. 39–67, Cambridge University Press.

Lumpkin, R. and S. L. Garzoli (2011), Interannual to Decadal Variability in the Southwestern Atlantic’s Surface Circulation, *J. Geophys. Res.-Oceans*, *116*, C01014, doi:10.1029/2010JC006285.

Lumpkin, R., S. Grodsky, L. Centurioni, M.-H. Rio, J. Carton and D. Lee (2012), Removing spurious low-frequency variability in drifter velocities, *J. Atmos. Oceanic Technol.*, in revision [minor revisions necessary].

Lutjeharms, J. R. E. (2007). Three decades of research on the greater Agulhas Current, *Ocean Sci.*, *3*, 129–147, doi:10.5194/os-3-129-2007.

Mantua, N.J. and S.R. Hare, Y. Zhang, J.M. Wallace, and R.C. Francis (1997), A Pacific interdecadal climate oscillation with impacts on salmon production, *Bull. Am. Meteorol. Soc.*, *78*, 1069–1079.

Mason, E., F. Colas, and J. Pelegrí (2012), A Lagrangian study tracing water parcel origins in the Canary Upwelling System, *Scientia Marina*, *76(S1)*, 79–94, doi:10.3989/scimar.03608.18D.

Maximenko, N., P. Niiler, M.-H. Rio, O. Melnichenko, L. Centurioni, D. Chambers, V. Zlotnicki, and B. Galperin (2009), Mean dynamic topography of the ocean derived from satellite and drifting buoy data using three different techniques, *J. Atmos. Oceanic Technol.*, *26*, 1910–1919, doi:10.1175/2009JTECHO672.1

Maximenko, N., J. Hafner, and P. Niiler (2012), Pathways of marine debris derived from trajectories of Lagrangian drifters, *Mar. Pollut. Bull.*, *65*, 51–62,

738 doi:10.1016/j.marpolbul.2011.04.016.

739 McCord, M. R., Y. K. Lee, and H. K. Lo (1999), Ship routing through altimetry-derived
740 ocean currents, *Transport. Sci.*, 33, 49–67, doi:10.1287/trsc.33.1.49.

741 Molinari, R. L., and J. Morrison (1988), The separation of the Yucatan Current from the
742 Campeche Bank and the intrusion of the Loop Current into the Gulf of Mexico, *J.*
743 *Geophys. Res.*, 93, 10,645–10,654, doi:10.1029/JC093iC09p10645.

744 Nagura, M., and M. J. McPhaden (2010), Wyrтки Jet dynamics: Seasonal variability, *J.*
745 *Geophys. Res.*, 115, C07009, doi:10.1029/2009JC005922.

746 Niiler, P. P. (2001), The world ocean surface circulation, in *Ocean Circulation and*
747 *Climate*, International Geophysics Series, 77, edited by G. Siedler, J. Church, and J.
748 Gould, pp. 193–204, Academic Press.

749 Niiler, P. P., A. Sybrandy, K. Bi, P. Poulain, and D. Bitterman (1995), Measurements of
750 the water-following capability of holey-sock and TRISTAR drifters, *Deep Sea Res.*,
751 42, 1951–1964.

752 Niiler, P. P. and J. D. Paduan (1995), Wind-driven motions in the northeast Pacific as
753 measured by Lagrangian drifters, *J. Phys. Oceanogr.* 25, 2819-2830.

754 Nykjær, L., and L. Van Camp (1994), Seasonal and interannual variability of coastal
755 upwelling along northwest Africa and Portugal from 1981 to 1991, *J. Geophys. Res.*,
756 99, 14,197–14,207, doi:10.1029/94JC00814.

757 Orsi, A. H., T. Whitworth III and W. D. Nowlin, Jr., (1995), On the meridional extent
758 and fronts of the Antarctic Circumpolar Current, *Deep-Sea Res. I*, 42, 641–
759 673. Palacios, D. M. and S. J. Bograd (2005), A census of Tehuantepec and Papagayo
760 eddies in the northeastern tropical Pacific, *Geophys. Res. Lett.*, 32, 23606, doi:

761 10.1029/2005GL024324.
 762 Pazan, S. E., and P. P. Niiler (2001), Recovery of near-surface velocity from undrogued
 763 drifters, *J. Atmos. Oceanic Technol.*, *18*, 476–489.
 764 Perez, R. C., M. F. Cronin and W. S. Kessler (2010), Tropical Cells and a Secondary
 765 Circulation near the Northern Front of the Equatorial Pacific Cold Tongue, *J. Phys.*
 766 *Oceanogr.*, *40*, 2091–2106.
 767 Potemra, J. T., and N. Schneider (2007), Interannual variations of the Indonesian
 768 throughflow, *J. Geophys. Res.*, *112*, C05035, doi:10.1029/2006JC003808.
 769 Poulain, P.-M., R. Gerin, E. Mauri, and R. Pennel (2009), Wind effects on drogued and
 770 undrogued drifters in the eastern Mediterranean, *J. Atmos. Oceanic Technol.*, *26*,
 771 1144–1156, doi:10.1175/2008JTECHO618.1.
 772 Provost, C., O. Garcia, and V. Garçon (1992), Analysis of satellite sea surface
 773 temperature time series in the Brazil-Malvinas Current confluence region: Dominance
 774 of the annual and semiannual periods, *J. Geophys. Res.*, *97*, 17,841–17,858,
 775 doi:10.1029/92JC01693.
 776 Qu, T., H. Mitsudera, and B. Qiu (2001), A climatological view of the Kuroshio/Oyashio
 777 system east of Japan, *J. Phys. Oceanogr.*, *31*, 2575–2589, doi:10.1175/1520-
 778 0485(2001)031<2575:ACVOTK>2.0.CO;2.
 779 Qu, T., H. Mitsudera, and T. Yamagata (1999), A Climatology of the Circulation and
 780 Water Mass Distribution near the Philippine Coast, *J. Phys. Oceanogr.*, *29*, 1488–
 781 1505.
 782 Reed, R.K. (1984), Flow of the Alaskan Stream and its variations, *Deep-Sea Res.*, *31*,
 783 369–386, doi:10.1016/0198-0149(84)90090-6.

784 Richardson, P. L., and D. Walsh (1986), Mapping climatological seasonal variations of
 785 surface currents in the tropical Atlantic using ship drifts, *J. Geophys. Res.*, *91*,
 786 10,537–10,550, doi:10.1029/JC091iC09p10537.

787 Richardson, P. L. (2005), Caribbean Current and eddies as observed by surface drifters,
 788 *Deep-Sea Res.*, *52*, 429–463, doi:10.1016/j.dsr2.2004.11.001.

789 Ridgway K.R., J.R. Dunn, and J.L. Wilkin (2002), Ocean interpolation by four-
 790 dimensional least squares -Application to the waters around Australia, *J. Atmos.*
 791 *Oceanic Technol.*, *19*, 1357–1375.

792 Rio, M. H., S. Guinehut, and G. Larnicol (2011), New CNES-CLS09 global mean
 793 dynamic topography computed from the combination of GRACE data, altimetry and
 794 in situ measurements, *J. Geophys. Res.*, *116*, C07,018, doi:10.1029/2010JCOO6505.

795 Risien, C. M., and D. B. Chelton (2008), A global climatology of surface wind and wind
 796 stress fields from eight years of QuikSCAT scatterometer data, *J. Phys. Oceanogr.*,
 797 *38*, 2379–2413, doi: 10.1175/2008JPO3881.1.

798 Rodrigues, R. R., L. M. Rothstein, and M. Wimbush (2007), Seasonal variability of the
 799 South Equatorial Current bifurcation in the Atlantic Ocean: A numerical study, *J.*
 800 *Phys. Oceanogr.*, *37*, 16–30.

801 Schmitz, W. J., Jr., and M. S. McCartney (1993), On the North Atlantic Circulation, *Rev.*
 802 *Geophys.*, *31*, 29–49, doi:10.1029/92RG02583.

803 Schott, F. A., and J. P. McCreary, Jr. (2001), The monsoon circulation of the Indian
 804 Ocean, *Prog. Oceanogr.*, *51*, 1–123.

805 Schott, F. A., J. P. McCreary, Jr., and G. C. Johnson (2004), Shallow overturning
 806 circulations of the tropical-subtropical oceans, in *Earth Climate: The Ocean-*

Atmosphere Interaction, C. Wang, S.-P. Xie, and J. A. Carton, Eds., American
 Geophysical Union Geophysical Monograph 147, 261–304.

Schott, F., J. C. Swallow, and M. Fieux (1990), The Somali current at the equator: annual
 cycle of currents and transports in the upper 1000 m and connection to neighbouring
 latitudes, *Deep-Sea Res. A*, *37*, 1825–1848, doi:10.1016/0198-0149(90)90080-F.

Sloyan, B. M., and S. R. Rintoul (2001). The Southern Ocean limb of the global deep
 overturning circulation, *J. Phys. Oceanogr.*, *31*, 143–173, doi:10.1175/1520-
 0485(2001)031<0143:TSOLOT>2.0.CO;2.

Stammer, D. (1997), Global characteristics of ocean variability estimated from regional
 TOPEX/POSEIDON altimeter measurements, *J. Phys. Oceanogr.*, *27*, 1743–1769.
 doi:10.1175/1520-0485(1997)027<1743:GCOOVE>2.0.CO;2

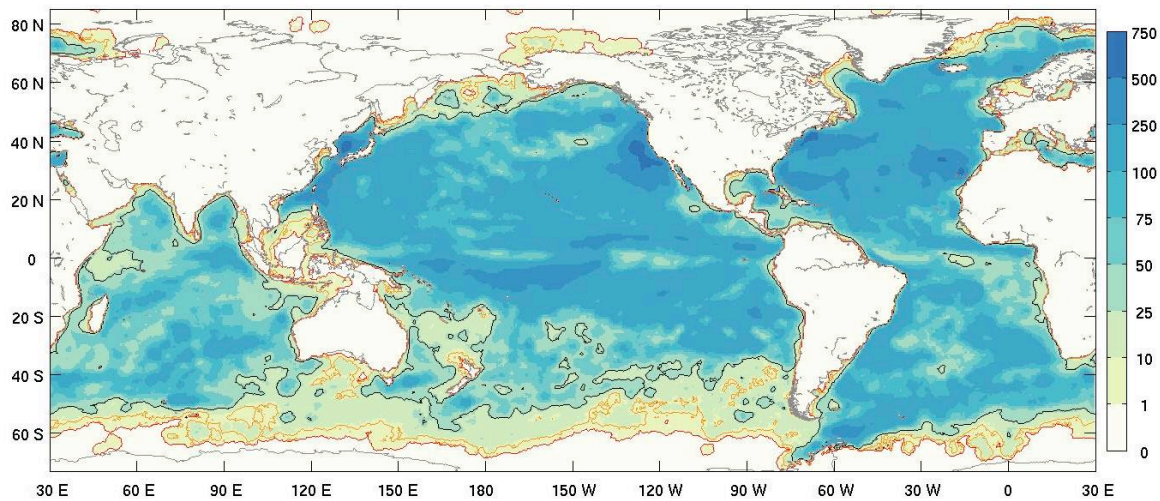
Swallow, J., M. Fieux, and F. Schott (1988), The Boundary Currents East and North of
 Madagascar 1. Geostrophic Currents and Transports, *J. Geophys. Res.*, *93*, 4951–
 4962, doi:10.1029/JC093iC05p04951.

Thompson, D. W. J., and J. M. Wallace (2000), Annular modes in the extratropical
 circulation. Part I: Month-to-month variability, *J. Climate*, *13*, 1000–1016.

Toole, J. M., R. C. Millard, Z. Wang, and S. Pu (1990), Observations of the Pacific North
 Equatorial Current bifurcation at the Philippine coast, *J. Phys. Oceanogr.*, *20*, 307–
 318, doi:10.1175/1520-0485(1990)020<0307:OOTPNE>2.0.CO;2.

Trenberth, K. E. (1984), Signal versus noise in the Southern Oscillation, *Mon. Weath.*
Rev., *112*, 326–332.

828 van Sebille, E., M. H. England and G. Froyland (2012), Origin, dynamics and evolution
 829 of ocean garbage patches from observed surface drifters, *Environ. Res. Lett.* 7,
 830 044040, doi:10.1088/1748-9326/7/4/044040.
 831 Wunsch, C. (1996), *The Ocean Circulation Inverse Problem*, Cambridge University
 832 Press, New York.
 833 Wunsch, C. (1998), The Work Done by the Wind on the Oceanic General Circulation, *J.*
 834 *Phys. Oceanogr.*, 28, 2332–2340.
 835 Yoder, J. A., S. G. Ackleson, R. T. Barber, P. Flament, and W. M. Balch (1994), A line
 836 in the sea, *Nature*, 371, 689–692, doi:10.1038/371689a0.
 837



838

839 Figure 1. Number of drogued drifter observations used to map fields at each grid point
 840 bin (in drifter days per square degree). Thresholds for estimating a mean field (0.8 drifter
 841 days per square degree, red), a seasonal cycle (7 days per square degree, orange), and a
 842 SOI regression (29 days per square degree, black) are contoured.

843

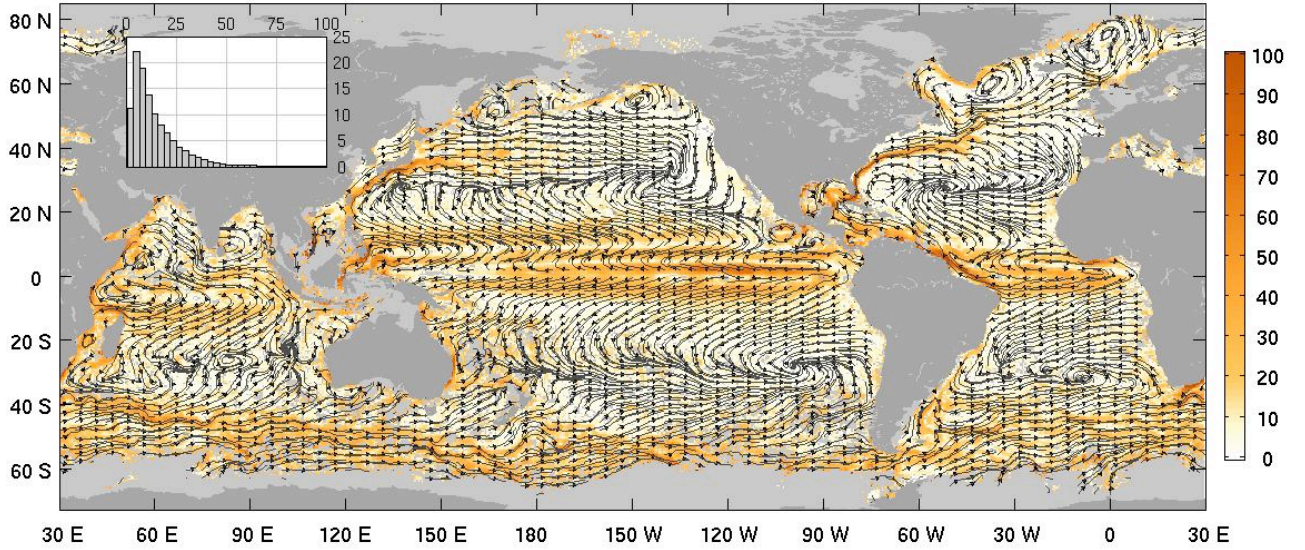


Figure 2. Mean current speeds (colors, in cm s^{-1}) from near-surface surface drifter data with streamlines (black lines). Streamlines are calculated from spatially smoothed currents to indicate flow direction and qualitatively illustrate large-scale circulation features, including surface divergence. Light gray areas have less than 10 drifter days per bin (0.8 per square degree). In addition, only bins with mean current speeds statistically different from zero at one standard error of the mean are shaded. Inset (top left) shows histogram of mean current speed (cm s^{-1} , horizontal axis, from 0 to 100) vs. number of bins (in kilobins, vertical axis, from 0 to 25,000 bins).

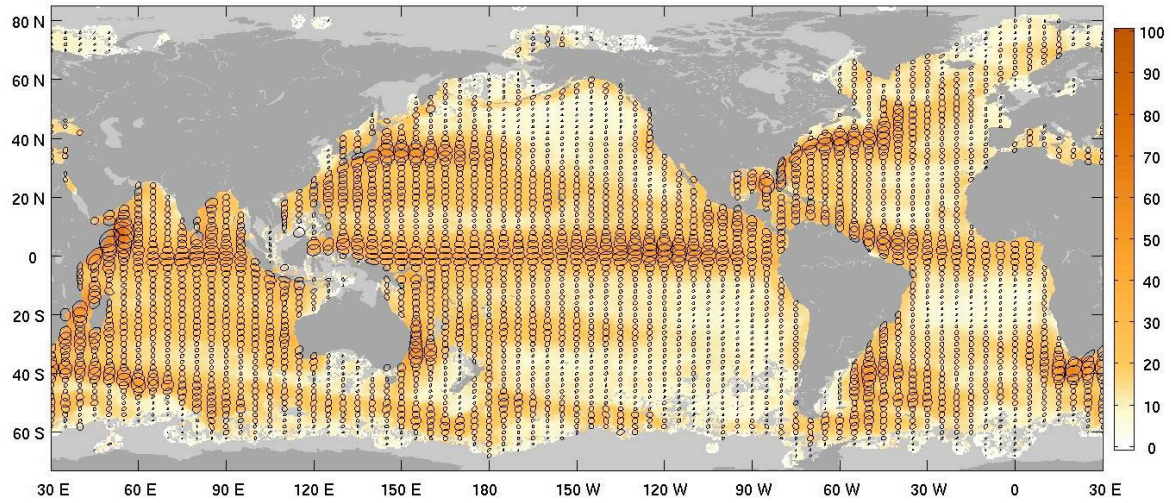
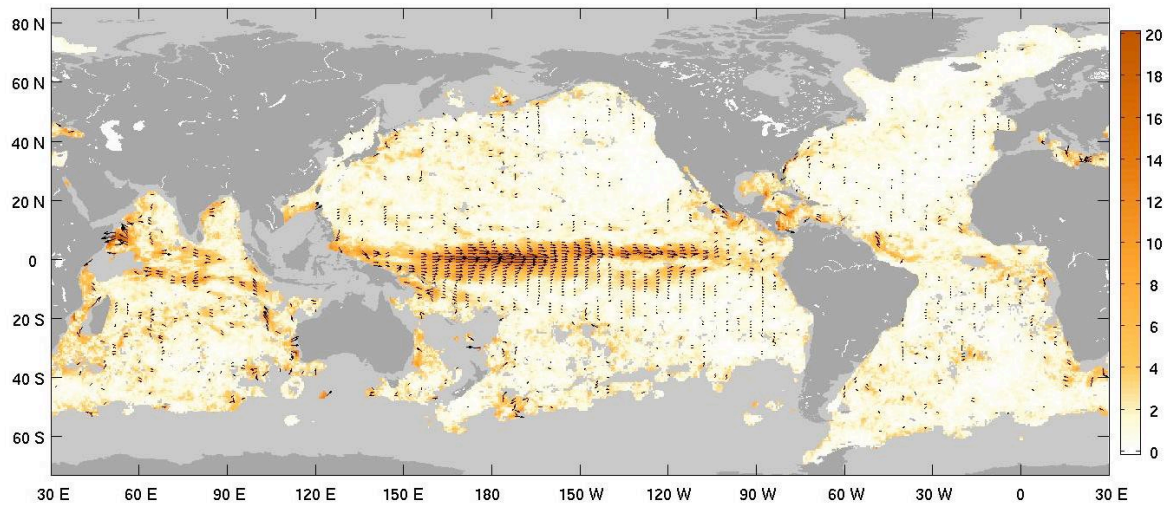


Figure 3. Variance ellipses centered every 5° longitude by 2° latitude (black lines) over the square root of the magnitude of variance (colors in cm s^{-1}). Light gray areas have less than 0.8 drifter days per square degree.

856



857

858 Figure 4. Speed of currents regressed onto the Southern Oscillation Index (colors in cm s^{-1}) shown for SOI = -1 (moderate El Niño) with directions (black arrows) indicated for a
859 subset of gridpoints. Arrows not shown where magnitude is not significantly different
860 from zero. Light gray areas have less than 365 drifter days per bin (29 per square
861 degree).
862

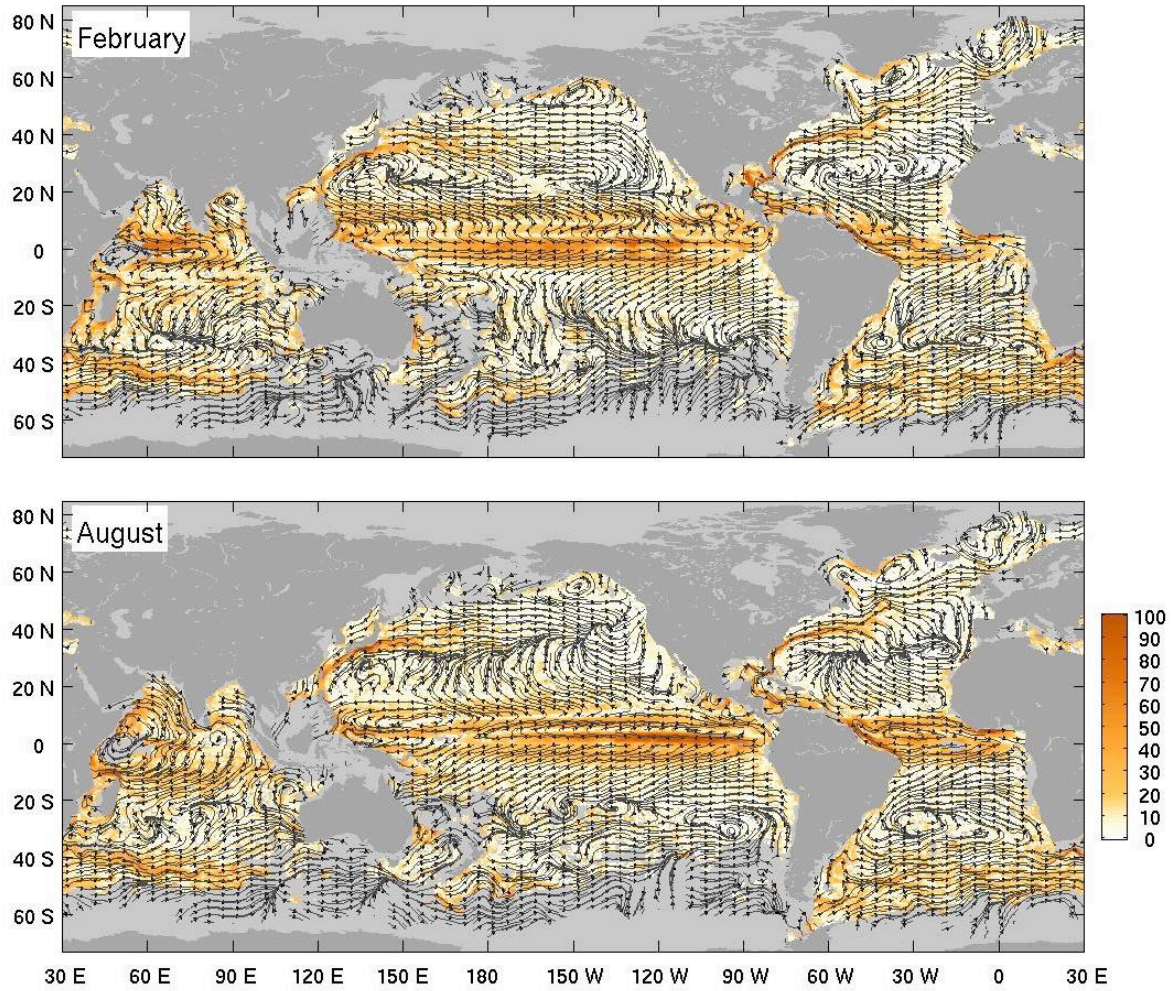
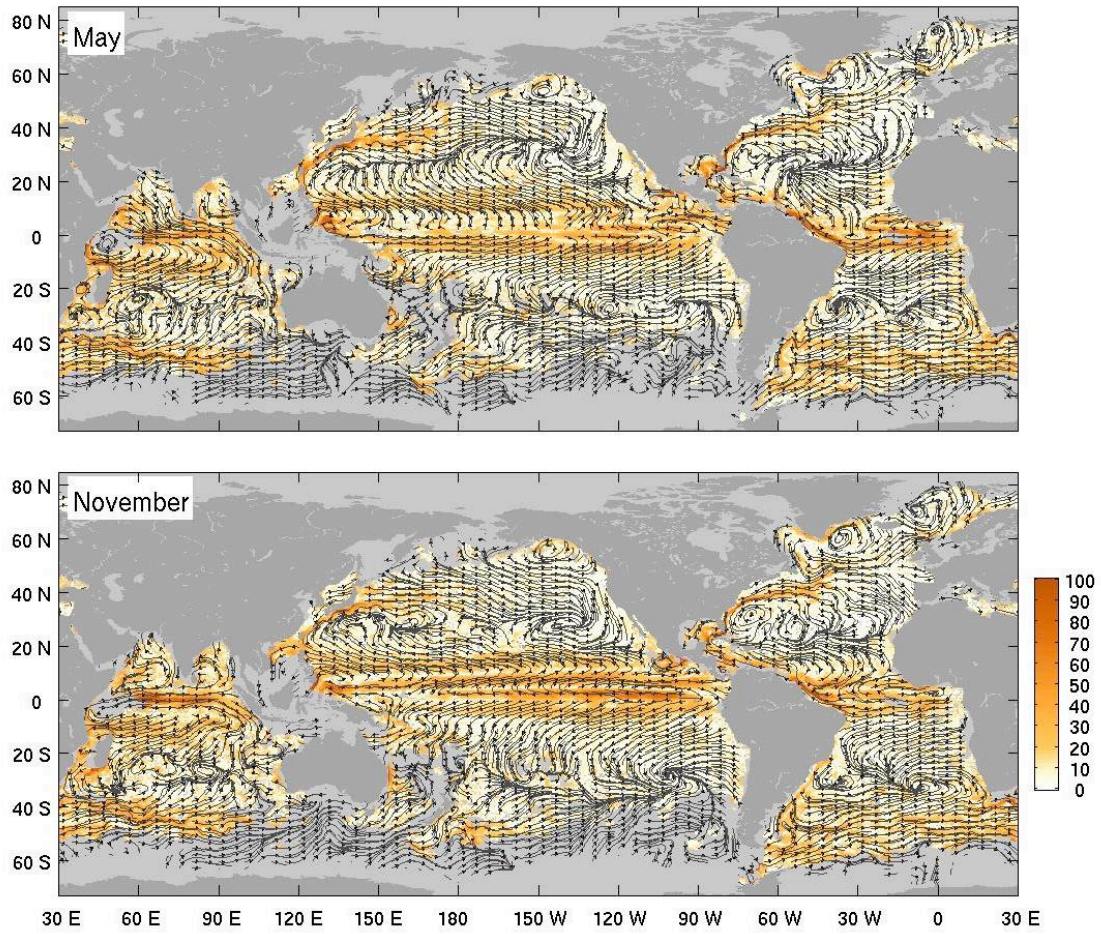


Figure 5. Near-surface ocean currents from surface drifter data. Details follow Figure 2, except displayed for climatological February (top panel) and August (bottom panel). Light gray areas have less than 90 drifter days per bin (7 per square degree).

867



868

869 Figure 6. Near-surface ocean currents from surface drifter data. Details follow Figure 2,

870 except displayed for climatological May (top panel) and November (bottom panel).

871 Light gray areas have less than 90 drifter days per bin (7 per square degree).

872

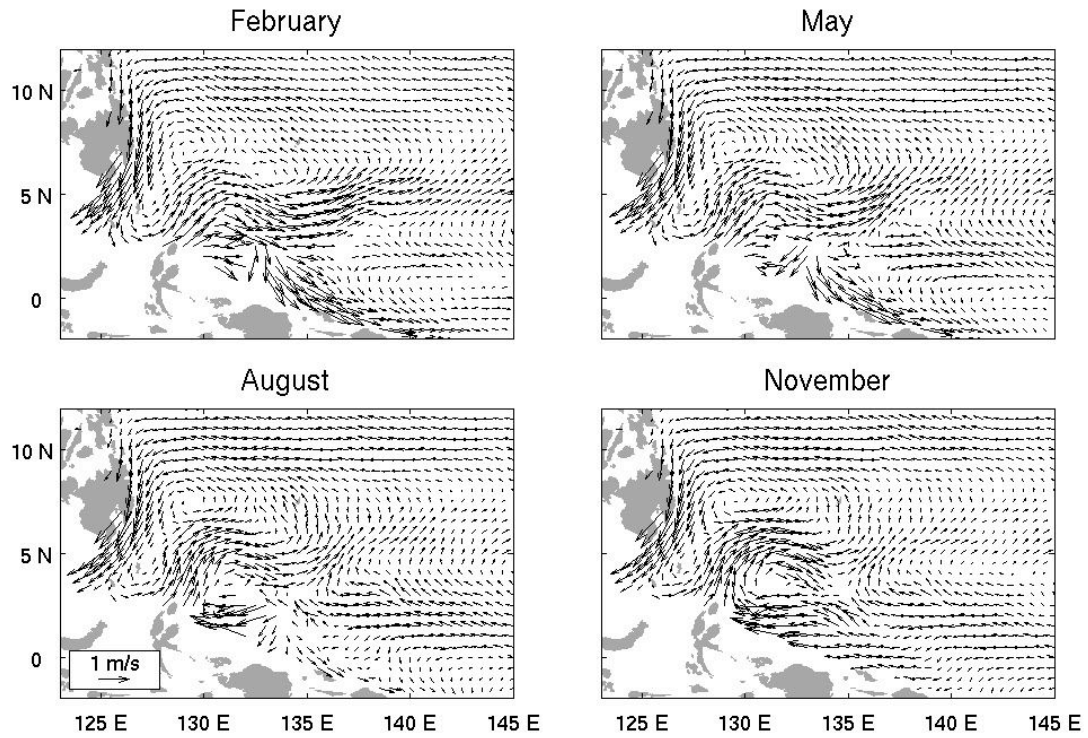


Figure 7. Seasonal variations of surface currents (black arrows, see key in lower left panel) in the northwestern tropical Pacific Ocean. Currents are not shown where they are not significantly different from zero at one standard error of the mean.

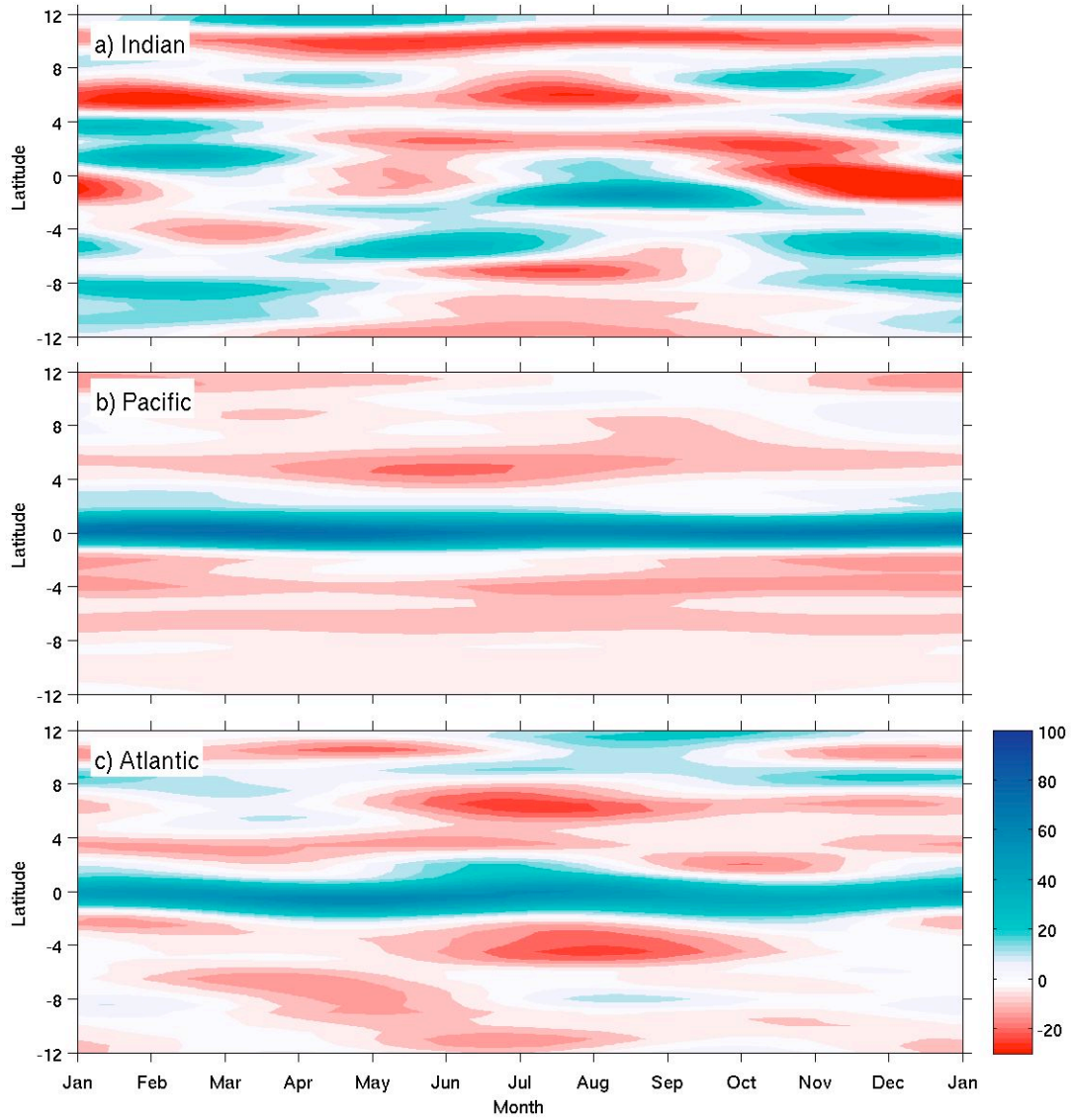


Figure 8. Seasonal cycle of surface divergence (colors, 10^{-8} s^{-1}) vs. latitude averaged over longitude bands in the interior of the a) Indian ($90^{\circ}\text{E} - 55^{\circ}\text{E}$), b) Pacific ($165^{\circ}\text{E} - 85^{\circ}\text{W}$), and c) Atlantic ($30^{\circ}\text{W} - 5^{\circ}\text{E}$) Oceans. Tick marks show the start of named months.

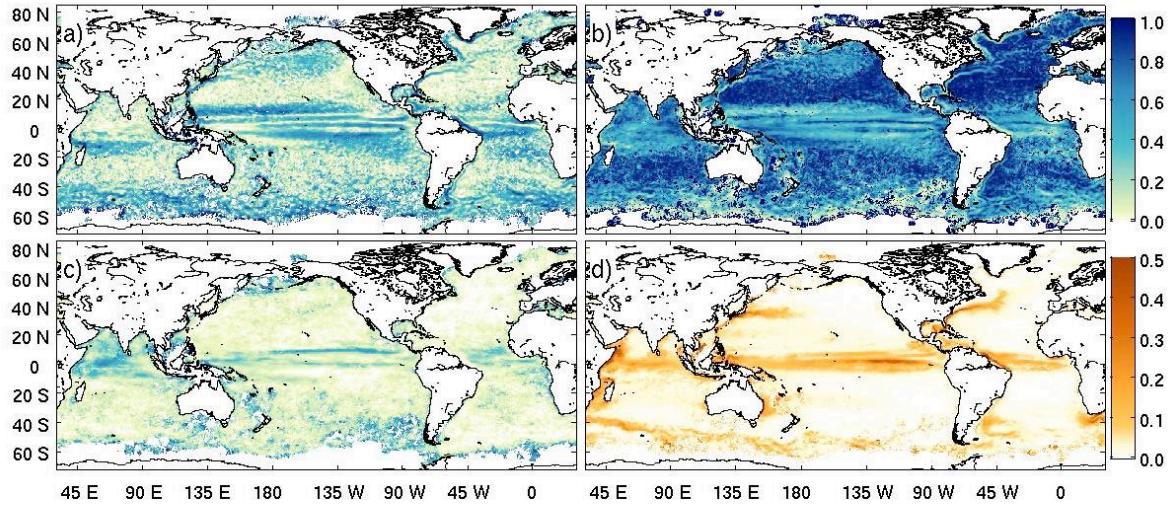


Figure 9. Fractions (colors, upper colorbar) of (a) time-mean, (b), eddy, and (c) seasonal contributions to the total surface kinetic energy in the drifter climatology along with (d) the total kinetic energy (colors, $\text{m}^2 \text{s}^{-2}$, lower colorbar).

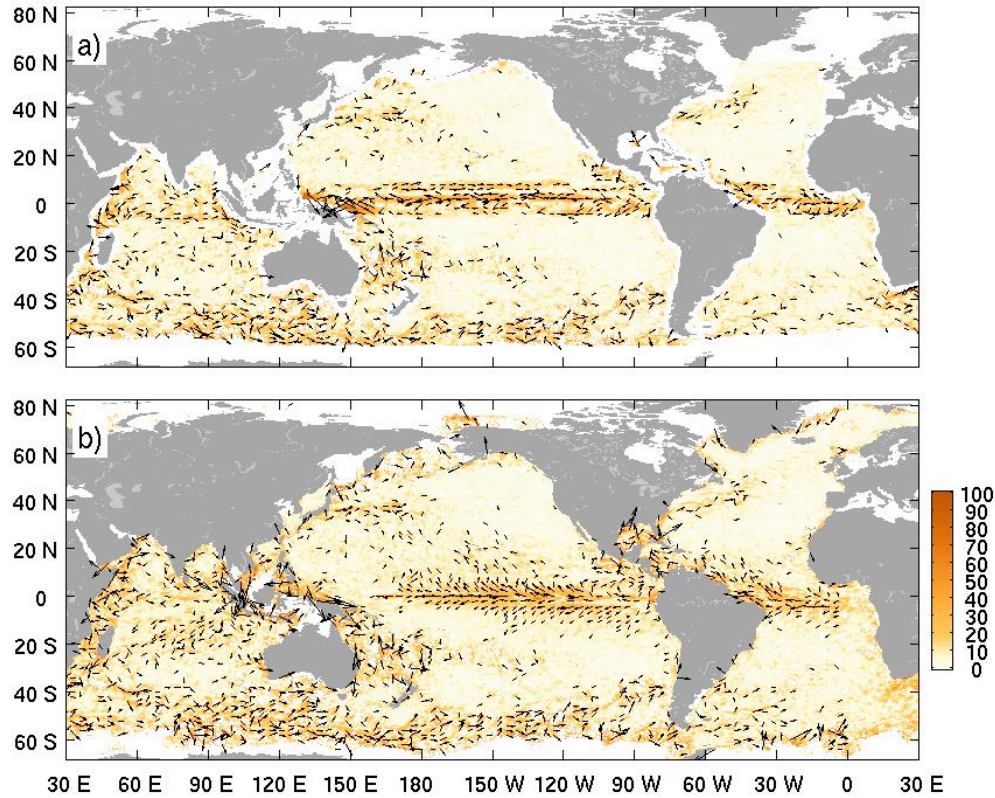


Figure 10. Vector differences (arrows; colors indicate difference magnitudes in cm s^{-1}), of a) time-mean velocity of drifters minus January 1993–December 2003 time-mean total speed from NOAA's 1/3 degree unsmoothed Ocean Surface Current Analysis Real-time (OSCAR) product [Bonjean and Lagerloef, 2002] including geostrophic, Ekman and buoyancy components, and b) time-mean velocity of drifters minus time-mean geostrophic speed from the CNES-CLS 2009 v1.1 Mean Dynamic Topography [Rio et al., 2011].

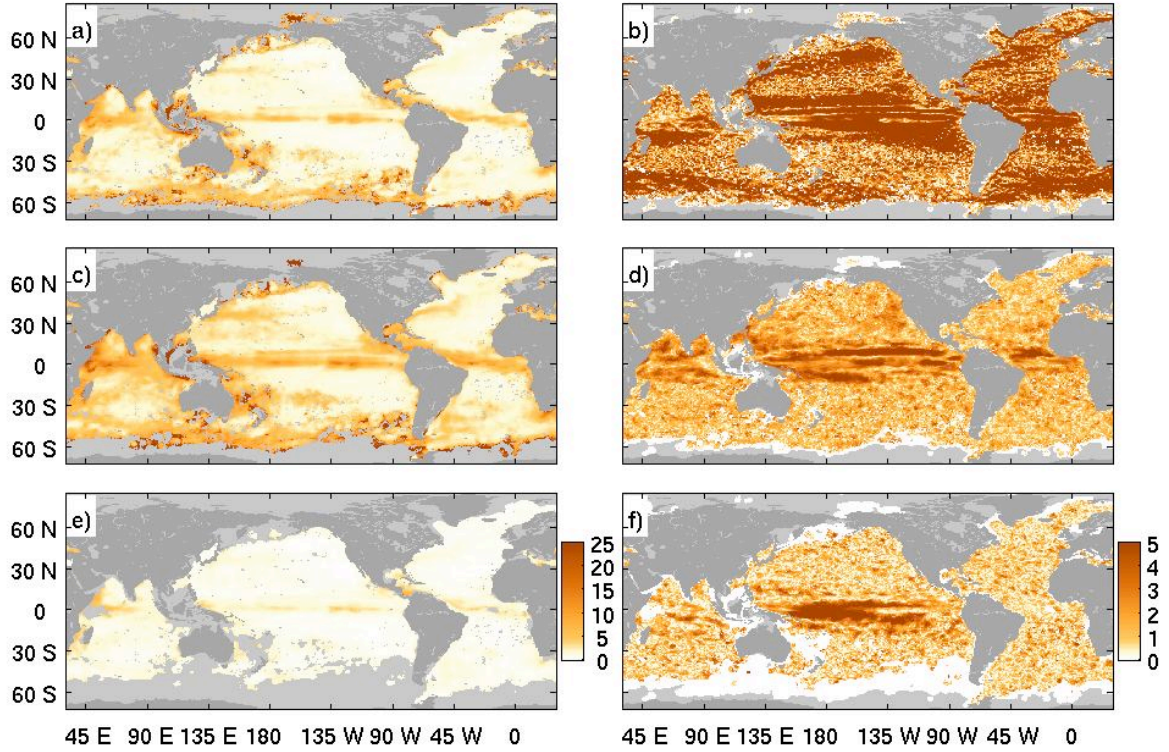


Figure 11: Left column: absolute error (square root of the sum of the squared errors) in
 (a) time-mean speed, (c) speed of seasonal variations (annual and semiannual) and (e)
 SOI-correlated currents (cm s^{-1} ; color bar adjacent to e). Right column: signal-to-noise
 ratio, i.e., magnitude of the coefficient (or square root of the sum of the squared
 coefficients) divided by the error estimates, for (b) absolute speed, (d) speed of seasonal
 variations, and (f) SOI-correlated currents (color bar adjacent to f).